Multimodal FACED imaging for large-scale single-cell morphological profiling

Cite as: APL Photon. 6, 070801 (2021); doi: 10.1063/5.0054714
Submitted: 21 April 2021 • Accepted: 11 June 2021 •
Published Online: 1 July 2021

Gwinky G. K. Yip,[1] Michelle C. K. Lo,[1] Wenwei Yan,[2,3] Kelvin C. M. Lee,[1] Queenie T. K. Lai,[1] Kenneth K. Y. Wong,[1,4] and Kevin K. Tsia[1,4,a)]

AFFILIATIONS

[1] Department of Electrical and Electronic Engineering, The University of Hong Kong, Pokfulam Road, Hong Kong
[2] Laboratory for Functional Optical Imaging, Department of Biomedical Engineering, Columbia University, New York, New York 10027, USA
[3] Mortimer B. Zuckerman Mind Brain Behavior Institute, Columbia University, New York, New York 10027, USA
[4] Advanced Biomedical Instrumentation Centre, Hong Kong Science Park, Shatin, New Territories, Hong Kong

[a)] **Author to whom correspondence should be addressed:** tsia@hku.hk

ABSTRACT

Free-space angular-chirp-enhanced delay (FACED) is an ultrafast laser-scanning technique that allows for high imaging speed at the scale orders of magnitude greater than the current technologies. However, this speed advantage has only been restricted to bright-field and fluorescence imaging—limiting the variety of image contents and hindering its applicability in image-based bioassay, which increasingly demands rich phenotypic readout at a large scale. Here, we present a new high-speed quantitative phase imaging (QPI) based on time-interleaved phase-gradient FACED image detection. We further integrate this system with a microfluidic flow cytometer platform that enables synchronized and co-registered single-cell QPI and fluorescence imaging at an imaging throughput of 77 000 cells/s with sub-cellular resolution. Combined with deep learning, this platform empowers comprehensive image-based profiling of single-cell biophysical phenotypes that can offer not only sufficient label-free power for cell-type classification but also cell-cycle phase tracking with high accuracy comparable to the gold-standard fluorescence method. This platform further enables correlative, compartment-specific single-cell analysis of the spatially resolved biophysical profiles at the throughput inaccessible with existing QPI methods. The high imaging throughput and content given by this multimodal FACED imaging system could open new opportunities in image-based single-cell analysis, especially systematic analysis that correlates the biophysical and biochemical information of cells, and provide new mechanistic insights into biophysical heterogeneities in many biological processes.

I. INTRODUCTION

Recent advances in optical microscopy have opened an increasingly detailed window into visualizing and understanding how biological cells—the basic unit of biological systems—work and fail. This ability has fueled a momentous shift in the use of microscopy from qualitative biological examination to quantitative cellular "fingerprinting" (or profiling) based on the information-rich cell morphology (e.g., rare cell detection,[1] identification of immune cell subtypes,[2] cell cycle analysis,[3] etc.). Imaging-based profiling can thus be regarded as a powerful alternative to the standard molecular assays that delineate the functional cell states without costly, time-consuming, and laborious workflow (e.g., sequencing protocols). Among all imaging modalities, quantitative phase imaging (QPI) is an emerging tool in basic biology and clinical research because it allows for non-invasive quantification of high-resolution biophysical properties of cells (e.g., cell size, shape, mass density, and its subcellular distribution) derived from the quantitative phase images. Otherwise inaccessible in the gold-standard fluorescence microscopy,[4] cellular biophysical properties (or phenotypes) are proven to be effective to reconcile cellular heterogeneity and thus be salient biomarkers (can even be more accurate than the fluorescence markers) for cancer,[5] aging,[6] and drug screening,[7] to name a few.

Going beyond, several approaches further incorporated fluorescence imaging with 2D (or even 3D) QPI to enable simultaneous readout of both molecular information specific to the subcellular organelles/molecules (given by fluorescence contrast)

and biophysical information (derived from QPI).[8–12] However, it remains restricted in adopting these integrated QPI systems in the growing field of image-based profiling. It is mainly because these platforms lack the imaging throughput (e.g., in the number of cells per second) required to offer sufficient statistical power and establish faithful correlation and/or validation of biophysical phenotypes with the foundational molecular knowledge.

Building upon our recently developed ultrafast imaging technique (at 10 MHz linescan rate) called free-space angular-chirp-enhanced delay (FACED)[13] imaging, here, we demonstrate a high-throughput imaging flow cytometry (IFC) system that enables multimodal single-cell QPI and fluorescence imaging at a highly scalable imaging throughput up to almost 10^5 cells/s with sub-cellular resolution. The defining feature of this system is the ultrafast multiplexed readout of differential phase-contrast (DPC) encoded in the line array of foci, which is generated through the concept of "infinity-mirror." Extending from our previous approach in time-stretch imaging,[14] we leverage the temporal discreteness of the foci array in FACED to interleave different differential phase-contrast measurements in time pixel-by-pixel. In this way, QPI can be retrieved at high speed bypassing the interferometric measurements and the complex phase retrieval computation.[15] More importantly, such an ultrafast QPI operation is synchronized with fluorescence image capture. Hence, it allows us to capture QPI and fluorescence images of the same cell simultaneously at high throughput.

In this work, we first present the theory of FACED-QPI based on a wave-optics model, followed by the experimental characterization of the single-cell FACED image quality (in all the DPC, QPI, and fluorescence image contrasts) and validation of the quantitative phase accuracy. We then demonstrate the utility of the platform in conjunction with deep learning to perform label-free cell-type classification and label-free cell-cycle progression tracking. We further investigate the correlation between the subcellular information obtained from QPI and fluorescence images and seek to understand how the spatially resolved biophysical profiles of cells respond to cell cycle progression. Hence, empowered by its large-scale analytical power, FACED IFC could allow for systematic analysis on multi-scale single-cell properties (both biophysical and biochemical) and, more importantly, on their largely underexplored inter-relationships. Such correlative, multi-scale single-cell analysis, mostly uncharted in the current methods, would provide a more profound knowledge of biophysical phenotypic heterogeneities of single-cells and new mechanistic insights into many biological processes.

II. MATERIALS AND METHODS

A. Multimodal FACED imaging

The multimodal FACED IFC platform comprises three modules (Fig. 1; see Fig. S3 of the supplementary material for

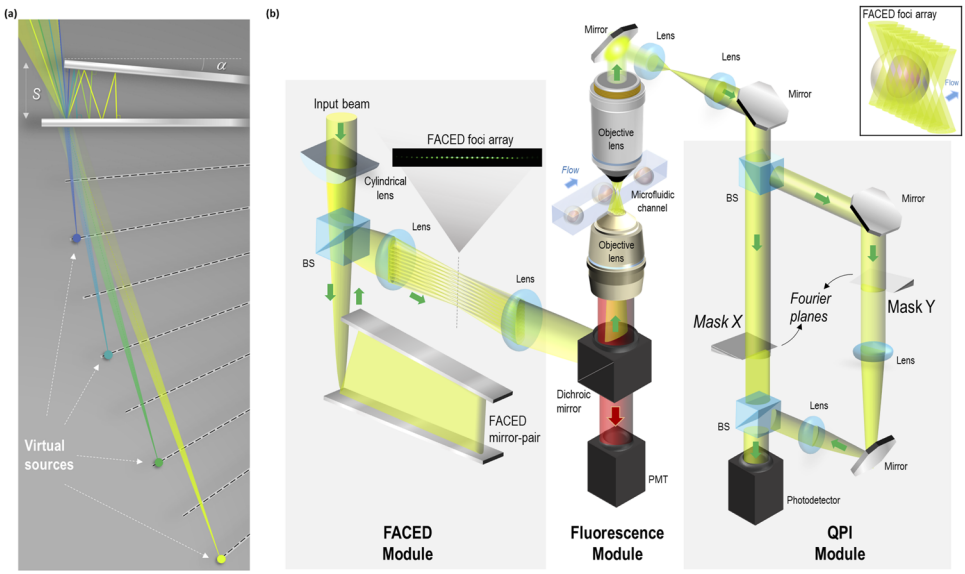

FIG. 1. Schematics of a multimodal FACED-IFC platform. (a) A ray-tracing diagram that describes the generation of the virtual source array by the mirror pair (with a separation S and tilt angle α). The FACED mirror-pair transforms a line-focusing pulsed laser beam [focused by a cylindrical lens shown in (b)] into a set of beamlets. Only four sources (color-coded) are shown for clarity. All beamlets follow different sets of multiple reflection paths and are then retroreflected along the identical paths. The returning beamlets can be regarded as light emerging from an array of virtual pulsed sources. (b) The overall system consists of three main modules: FACED, QPI, and fluorescence module. Because of the different path delays from different virtual sources, the beamlets generated by the FACED module form an array of spatially separated and temporally delayed foci onto an intermediate conjugate plane of the virtual sources (see the inset in the FACED module). These foci are further projected through intermediate optics of the systems onto the imaging plane of a microscope, forming an ultrafast line-scanning beam illuminated onto the flowing cells (see the inset at the top right corner for a zoom-in view). The fluorescence linescan signals emitted from the flowing cells are collected by using a high-speed PMT in the fluorescence module. The QPI module comprises a two-arm delay-line, which time-interleaves the two transmitted line-scan replicas, but with different differential phase-contrasts (DPCs) generated by two knife-edges at the Fourier planes of the image plane (masks X and Y, respectively) (see Fig. 2 for the detailed working principle). The interleaved line scans are then detected in real-time by using the high-speed photodetector. BS: beamsplitter. PMT: photomultiplier tube.

detailed setup configuration), which are introduced in Subsections II A 1–II A 3 in detail.

1. FACED module

FACED relies on the concept of "infinity mirror" that generates an array of laser foci at the line-scan rate at least 10–100 times faster than the existing galvo-mirror scanning methods. Simply composed of two plane (static) mirrors (mirror separation S = 150 mm, mirror length L = 200 mm, mirror angle tilt $\alpha < 1$ mrad, and mirror reflectivity >99.5% at 532 nm) and a cylindrical lens, a FACED module transforms a pulsed laser beam into a set of beamlets, each of which follows a unique multiple (zig-zig) light reflection path. The zig-zag reflections are progressively denser and are eventually retroreflected along the identical paths, but with different round trip time delays. In essence, the returning beamlets from the mirror pair manifest themselves as being emerged from a linear array of *virtual pulsed sources* [Fig. 1(a)]. Note that the temporal and spatial densities of virtual sources are reconfigurable by tuning the geometry of the mirror pair and the input light cone.[13] In this work, the number of virtual sources used for imaging is chosen to be $N = 50$ and the temporal separation between adjacent virtual sources is 1 ns. These virtual sources are projected through the intermediate optics onto the imaging plane as an ultrafast all-optical scanning illumination/excitation beam at a line-scan rate governed by the repetition rate of the mode-lock laser source ($1/T = 20$ MHz). Detailed principle of FACED can be referred to Ref. 13.

2. FACED-QPI module

a. Theory. Unlike the classical interferometric approaches that rely on complex field measurements, the phase retrieval algorithm used in this work is based on intensity-only measurements. The working principle is generally based on the fact that local phase gradient induced by the cells $[\vec{\nabla}\varphi(x,y)]$ causes wavefront tilt or local angle tilt $\vec{\theta}(x,y)$ for each spatiotemporally separated FACED focus beam,

$$\vec{\nabla}\varphi(x,y) = \frac{2\pi}{\lambda}\vec{\theta}(x,y). \tag{1}$$

λ is the illumination wavelength. Such a light tilt on the image plane, in turn, results in a transverse displacement of each FACED focus beam on the Fourier plane. Suppose that one partially blocks the light profile on the Fourier plane (e.g., by knife-edge) [Fig. 1(b)]. In that case, the resultant fractional intensity losses of each focus (which can be measured separately in real-time) can then be computationally linked to the phase-gradient and thus quantitative phase (Fig. 2).

To further illustrate the underlying theory, we consider only one of the FACED foci as the input illumination without loss of generality. Here, a knife-edge mask is placed at the Fourier plane of the sample plane to half-block the light profile along the x-direction. The light field $E_k(x_k, y_k)$ on the knife-edge plane can be related to the field at the sample plane, which is denoted as $E_s(x_s, y_s)$, by

$$E_k(x_k, y_k) \propto \frac{1 + sgn(x_k)}{2}\mathcal{F}(E_s(x_s, y_s)), \tag{2}$$

where $E_s(x_s, y_s)$ is proportional to both the input field amplitude profile $A(x_s, y_s)$ and the phase profile $\varphi(x_s, y_s)$ of the sample, i.e., $E_s(x_s, y_s) \propto A(x_s, y_s)\exp[-j\varphi(x_s, y_s)]$. Note that (x_s, y_s) and (x_k, y_k) are the coordinates on the sample plane and its Fourier plane, respectively. $\mathrm{sgn}(x_k)$ is the sign function along the x-direction representing the knife-edge (mask X) (Fig. 2), and $\mathcal{F}$ is the operator of 2D spatial Fourier transform.

Subsequently, the light is captured by using the free-space photodetector (PD) located at the conjugate plane of the sample plane. Hence, the detected light field $E_d(x_d, y_d)$ is proportional to

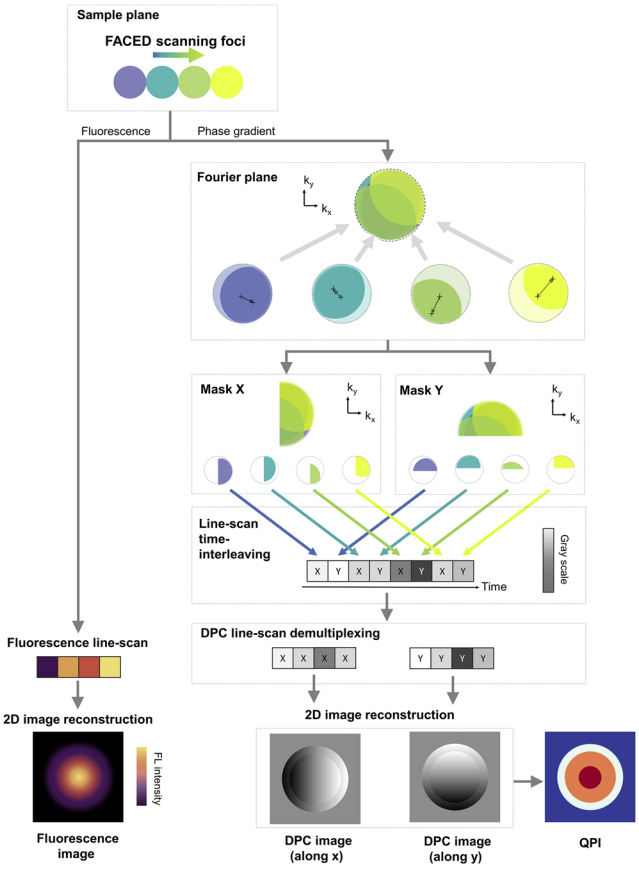

FIG. 2. The workflow of simultaneous FACED-QPI and fluorescence image reconstruction. The FACED foci {only four color-coded foci [the same as Fig. 1(a)] are shown for clarity} illuminate the flowing cells to generate two image contrasts simultaneously. (Left) 1D fluorescence line-scan signals. (Right) 1D phase-gradient line-scan signals. The 2D fluorescence image is reconstructed by digitally stacking the 1D fluorescence line scans. On the other hand, the transmitted beamlets encoded with the phase-gradient information of the cells are split into two replicas in the two delay arms [see Fig. 1(b)]. Note that the local phase-gradient experienced in each FACED beamlet is encoded as beamlet translation (both its direction and magnitude) on the Fourier plane (see the arrows indicating the translation of the four beamlets). By half-blocking the beam profiles at the Fourier planes on the two arms along the horizontal (mask X) and vertical direction (mask Y), respectively, the intensity loss of each beamlet is directly linked to the magnitude and direction of the beam translation and thus phase gradient. Hence, the two arms essentially generate two orthogonal DPC line scans $[\hat{I}_x(x,y)$ and $\hat{I}_y(x,y)]$, which are time-interleaved focus-by-focus (i.e., pixel-by-pixel) and detected by using a single-pixel photodetector. The linescan signals are demultiplexed by alternatively selecting the $\hat{I}_x(x,y)$ and $\hat{I}_y(x,y)$ linescan signals. After 2D reconstruction of the two DPC images (along x and y directions), QPI can be obtained by performing complex Fourier integration on the two DPC images based on Eqs. (4) and (5).

$\mathcal{F}(E_k(x_k, y_k))$, where (x_d, y_d) are the coordinates on the detector plane. Based on the smooth phase approximation, the integrated intensity at the detection plane can be evaluated as

$$I_x = \iint |E_d|^2 dx_d dy_d = C\frac{\partial \varphi}{\partial x_s} + B, \tag{3}$$

where B and C are the constants related to the input field. Note that the same derivation can be applied to the knife edge that half-blocks the light profile in the y-direction (mask Y). Equation (3) asserts that the phase-gradient information (along both the x- and y-directions) of the phase object (i.e., cell) can be derived from the intensity-only measurement in FACED-QPI. The measured intensity images from Eq. (3) are essentially DPC images along the two orthogonal directions. The detailed derivation can be referred to the supplementary material, Note 2.

In practice, the relationship between the DPC intensities and the phase gradient can experimentally be quantified through simple geometry that connects the DPC intensities and the local light tilt angle $\theta_x(x, y)$ and $\theta_y(x, y)$ along the x- and y-directions,

$$\begin{bmatrix} \theta_x(x,y) \\ \theta_y(x,y) \end{bmatrix} = -NA_i \begin{bmatrix} f^{-1}\left(\frac{\hat{I}_x(x,y)-1}{2}\right) \\ f^{-1}\left(\frac{\hat{I}_y(x,y)-1}{2}\right) \end{bmatrix}, \tag{4}$$

where $f\left(\frac{\Delta x}{r}\right) = \frac{\hat{I}_x(x,y)-1}{2}$ and $f\left(\frac{\Delta y}{r}\right) = \frac{\hat{I}_y(x,y)-1}{2}$. $f()$ is the function connecting the intensity changes to the transverse displacement (Δx and Δy along the x- and y-directions, respectively) of each FACED beamlet on the Fourier plane as a consequence of the local phase gradient on the sample plane. Detailed derivation of the function $f()$ can be referred to Note 3 of the supplementary material. NA_i is the numerical aperture of the illumination objective lens. $\hat{I}_x(x, y)$ and $\hat{I}_y(x, y)$ are the normalized DPC images with a partial beam block (masks X and Y in Fig. 2) along x and y directions, respectively. To ensure high computation efficiency in the phase reconstruction pipeline, the local light tilt angles in Eq. (4) are evaluated through a lookup table constructed based on $f()$ (see Note 3 of the supplementary material).

Combining Eqs. (1) and (4), one can, in principle, integrate $\vec{\nabla}\varphi(x, y)$ to obtain QPI, i.e., $\varphi(x, y)$. Here, we apply complex Fourier integration[16] on a complex phase gradient, which is defined as $g(x, y) = \frac{\partial \phi}{\partial x_s}(x, y) + i\frac{\partial \phi}{\partial y_s}(x, y)$. Hence, $\varphi(x, y)$ can be evaluated as

$$\varphi(x, y) = CF \cdot Im\{\mathcal{F}^{-1}\{NF \cdot \mathcal{F}[g(x, y)]\}\},$$

where

$$NF = \begin{cases} FOV/[2\pi j \cdot k(x, y)], & k(x, y) \neq 0 \\ 0, & k(x, y) = 0, \end{cases} \tag{5}$$

where CF is the calibration factor for correcting the systematic phase deviation arising from non-ideal system settings, e.g., optical aberration. Im is the imaginary part of a complex number, and $\mathcal{F}^{-1}$ is the operator of inverse Fourier transform. NF is the normalization factor for quantifying the phase. FOV is the field of view of the image determined by a grid target with known dimensions, and $k(x, y)$ is the spatial frequency. Note that as cells are generally transparent and weakly scattering, absorption and scattering losses are thus ignored in the phase retrieval algorithm. In practice, the noise in DPC images $[\hat{I}_x(x, y), \hat{I}_y(x, y)]$ is contributed by the laser intensity noise (mainly shot noise) and possibly the detector noise, especially in high-speed detection. These noise sources would eventually be translated to the phase noise in the FACED-QPI (see Figs. S4a and S4b of the supplementary material). By analyzing the background (cell-free) region of each single-cell phase image, we quantified the phase noise to be on the order of tens of mrad (see Fig. S4c of the supplementary material), which has a negligible impact on image-derived phenotyping and image analysis presented in this work.

b. QPI module and phase reconstruction pipeline. The critical attribute of FACED-QPI is its ultrafast phase retrieval operation. This is achieved by generating the two DPC images $[\hat{I}_x(x, y), \hat{I}_y(x, y)]$ of the same cell simultaneously in real-time based on a time-interleaving detection approach. The significant steps include the following: (1) Split the FACED pulsed beamlets (which have already been transmitted through the cells) into two paths by using a 50:50 beam splitter. (2) Place two knife-edge masks (denoted as masks X and Y) near the Fourier planes of the image plane along these two paths. As described earlier [Eq. (2)], the masks block half of the light profiles along two orthogonal directions (Fig. 1). It thus results in the image line scans exhibiting DPCs, i.e., mask X (or Y) creates DPC along the x-direction (or y-direction). (3) Introduce an additional path-length delay in one path for time-multiplexed detection of the DPC line scans. A similar time-multiplexing scheme has been applied to time-stretch QPI.[14] However, it requires the line-scan replicas to be completely separated in time and thus compromises the line-scan rate (and imaging speed). In contrast, leveraging the spatiotemporal discreteness of the virtual sources, we temporally interleaved the subpulses of two DPC line scans (each consists of N subpulses) (Fig. 2). Here, we set the time delay between two light paths to be approximately half of the temporal separation between adjacent FACED virtual sources, i.e., ~500 ps. This time-interleaving approach in FACED-QPI allows for multiplexed DPC detection without sacrificing the line-scan rate. As N = 50 virtual sources generated from the current FACED configuration, a total of $2N$ = 100 subpulses were all detected in one complete line scan (i.e., T = 50 ns), which consists of two temporally interleaved DPC line scans. The multiplexed signals were detected using a single photodetector (response time < 30 ps and bandwidth > 10 GHz, Alphalas) and were then digitized by using a real-time high-speed oscilloscope (20 GHz, 80 GS/s, Lecroy). (4) Digitally demultiplex the composite line scan by alternately sampling the peak amplitude of each FACED subpulse to reconstruct the line scan of DPC images $\hat{I}_x(x, y)$ or $\hat{I}_y(x, y)$, respectively. Note that both $\hat{I}_x(x, y)$ and $\hat{I}_y(x, y)$ are the normalized DPC images, which were obtained by normalizing the raw line scans by the background scan. Here, the background scan is referred to the averaged raw line scans of the cell-free regions. Finally, QPI was reconstructed based on Eqs. (4) and (5). In this work, the QPI reconstruction pipeline was performed offline by using a consumer-grade computer. In order to streamline this pipeline in real-time and at high throughput (10 000 cells/s), we have recently demonstrated an online continuous image processing workflow based on a high-performance computing platform using a field programmable gate array.[17,18]

c. Phase calibration. A quantitative phase target (Benchmark Technologies), which is a rectangular block with well-defined

height (250 nm) and refractive index (1.52) (see Fig. S5a of the supplementary material), was used for phase calibration. The image of the target was captured in the FACED imaging system by translating the target along the slow axis using a motorized actuator (with a step size of 0.5 μm). Figure S5b of the supplementary material shows the average height profile (computed based on the calibrated phase values) of the rectangular block, which is highly consistent with the manufacturer's specification, i.e., 250 nm.

3. Fluorescence imaging module

Simultaneously, with the QPI capture, the epi-fluorescence signals (from Vybrant DyeCycle orange, Invitrogen; peak emission wavelength: 575 nm) emitted from the same set of FACED excitation foci used for QPI were detected serially by using a high-speed photomultiplier tube (PMT) (rise time = 0.57 ns, Hamamatsu) after passing through a series of relay lenses and dichroic beam splitters (see Fig. S3 of the supplementary material). Individual 1D fluorescence line scans were detected synchronously with the multiplexed DPC line scan. The 2D fluorescence image of a single cell was reconstructed by stacking the 1D line-scan data. The acquisition of the DPC and fluorescence images was co-registered to the same cell and was synchronously acquired by using a real-time high-speed oscilloscope (20 GHz, 80 GS/s, Lecroy).

B. Neural network

1. Deep neural network-based cell-type classification

We first established a single-cell phenotypic profile consisting of a total of 51 spatially resolved biophysical features derived from each single-cell FACED-QPI. These features include the typical bulk parameters, e.g., cell size, circularity, and dry mass density (DMD), as well as the texture parameters, e.g., dry mass variance and other higher-order-moment statistics (see Table S1 of the supplementary material, Note 1, for detailed definition of each feature). The biophysical phenotypes of single cells were only extracted from cell body region, which was defined by a binary mask (based on the QPI) outlining the cell shape (see Table S2 of the supplementary material, Note 1). Note that we followed the hierarchical profiling strategy (from bulk to global and local texture) that has been shown effective to capture the spatial characteristics of single cells holistically.[19] We next trained a deep neural network model to classify two breast cancer cell types (MDA-MB231 and MCF7), entirely based on the input knowledge given by the single-cell biophysical profiles. The neural network model is composed of three fully connected hidden layers, each with 100, 50, and 25 nodes, respectively, and connected with a rectified linear unit as activation functions. The 51-dimensional biophysical profile (i.e., consisting of 51 features), normalized based on the z-score, was used as the input of the model. The softmax function was implemented at the output layer, and the cross-entropy function was used as the loss function. Tenfold validation was performed to avoid overfitting. To examine the classification performance, a confusion matrix is generated to show the accuracy of classification. A dataset with 8705 cells (4391 cells from MDA-MB231 and 4314 cells from MCF7) was employed, and 90% of the dataset per cell line was used to train the classification model, whereas the remaining batch was used as the test set (repeated for ten times). The model was first trained with the training set for 300 epochs at a learning rate of 0.0001 with a mini-batch size of 128. Python was employed to develop the classification model in a consumer-grade computer with a CPU (6 cores, 12 threads; 4.00 GHz), a 64 GB RAM. The detailed network architecture can be referred to the supplementary material, Fig. S6a.

2. Cell cycle analysis

In the cell-cycle prediction experiments, we used the QPI as inputs to train and test a convolutional neural network (CNN) based model to predict DNA content. The ground truth of the DNA content is given by the DNA fluorescence dye labeled to the cells (Vybrant DyeCycle orange, Invitrogen) and is thus read out from the FACED fluorescence images. To train the model, half of the dataset per cell line was used as a training dataset, and mean squared error was used as a loss function with the Adam optimization algorithm. The model was first trained with the training set for 300 epochs at a learning rate of 0.000 001 and with a mini-batch size of 15. A test set was then employed to examine the performance of the model. The CNN-based regression model was composed of multiple 2D convolution layers, batch normalization layers, and leaky rectified linear units. At the output layer, a linear activation function was used to predict the normalized fluorescent intensity of cells, which was indicative of the cell cycle status. The detailed CNN architecture can be referred to the supplementary material, Fig. S6b. We also applied the Watson pragmatic curve-fitting on the fluorescence (DNA content) histogram[20] given by the FACED fluorescence image data to estimate the probability distributions for the cells (both MDA-MB231 and MCF7) belonging to the G1, S, and G2/M phases of the cell cycle.

C. Microfluidic channel fabrication

The microfluidic channel [made of polydimethylsiloxane (PDMS)] used in this work was designed to form an in-focus stream of single cells under high-speed microfluidic flow (>2 m/s) based on inertial focusing. The key fabrication steps are described as follows: First, a negative photoresist (SU-82025, MicroChem, US) was poured onto a silicon wafer, and a spin coater (spinNXG-P1, Apex Instruments Co., India) was used to coat the photoresist on the wafer. After soft baking at 65 °C for 3 min and then 95 °C for 6 min to remove the solvent, the wafer was cooled down under room temperature. Then, a target computer-aided design (CAD) pattern was transferred onto the photoresist by using a maskless soft lithography machine (SF-100 XCEL, Intelligent Micro Patterning, LLC, US) with exposure for 4 sec, followed by post-exposure bake at 65 °C for 1 min and then 95 °C for 6 min for further polymerization. After that, the SU-8 developer (MicroChem, US) was used for development of photoresist for 5 min. After rinsing and drying the wafer with isopropyl alcohol and pressurized air, respectively, the mixed solution of the PDMS precursor (SYLGARD® 184 Silicone Elastomer kit, Dow Corning, US) and curing agent (with a mix ratio of 10:1) was poured onto the wafer mold. The channel height of the imaging section was controlled by placing a homemade acrylic block on the wafer, followed by curing of the channel inside an oven operating at 65 °C for 2 h before demolding. By using a biopsy punch (Miltex 33-31 AA, Integra LifeSciences, US), two holes were then punched on the inlet and outlet of the channel for insertion of plastic tubing (BB31695-PE/2, Scientific Commodities, Inc., US). After bonding a glass slide to the channel by using oxygen plasma (PDC-002, Harrick

Plasma, US), the whole channel was baked inside an oven operating at 65 °C for 30 min for strengthening the bonding. Before carrying out the experiment, plastic tubings were inserted into the punched holes for the flow of the cell suspension into the channel. The channel dimensions at the imaging section were 30 μm in height and 60 μm in width.

D. Cell culture

The cancer cell lines used in this work, including two breast cancer cell lines MDA-MB231 and MCF7, and one human leukemic monocyte cell line, THP-1, were purchased from American Type Culture Collection (ATCC). They were cultured in the tissue culture flasks (surface area of 75 cm^2) (TPP) and incubated under 37 °C and 5% CO_2. For MDA-MB231, the full culture medium was ATCC modified RPMI 1640 (Gibco) containing 10% fetal bovine serum (FBS) (Gibco) and 1% antibiotic–antimycotic (Anti–Anti) (Gibco). For MCF-7, the full culture medium was DMEM (Gibco) containing 10% FBS (Gibco) and 1% Anti–Anti (Gibco). For THP-1, the full culture medium was the full medium for MDA-MB231 with 50 μl of 2-mercaptoethanol added for every 50 ml of medium. The cells were subcultured 2 to 3 times per week according to the cell confluency observed under a standard light microscope.

E. Cell preparation

For the experiments of cell-type classification and cell-cycle progression study, ~1 × 10^6 cells were extracted from each of the breast cancer cell lines and suspended in 1 ml of 1X PBS. Next, 0.5 μl of Vybrant DyeCycle orange stain (Invitrogen) was mixed with 4.5 μl of 1X PBS for dilution, and 2 μl of the mixed solution is added to the 1 × 10^6 cells. Then, the cells are incubated at 37 °C for 30 min. Afterward, the full medium was added to the cell suspension such that the total volume of 3 ml was obtained for the subsequent imaging experiments.

III. RESULTS

A. Imaging performance of multimodal FACED IFC

We first demonstrated the general imaging capability of synchronized single-cell quantitative phase and fluorescence FACED image capture in the high-speed microfluidic flow configuration. We employed three different cell types, which include human leukemic monocyte (THP-1) and breast cancer cells (MDA-MB231 and MCF7) for this test (Fig. 3). Under the ultrafast imaging rate (a line-scan rate of 20 MHz), this multimodal FACED IFC platform enabled high-throughput image capture of individual fast-flowing cells (~77 000 cells/s), revealing multiple image contrasts with subcellular resolution (i.e., the two DPCs, QPI, and fluorescence images) simultaneously. Note that this imaging throughput is at least two orders of magnitude higher than the existing QPI systems that also combine with fluorescence imaging capability. Hence, such a high throughput together with the subcellular image resolution critically enables large-scale, information-rich single-cell image-based analysis that not only harnesses the bulk cellular features (e.g., cell size and mass) but also further quantifies subcellular biophysical features of single cells—the single-cell phenotypic profile inaccessible in the current IFC systems.

B. Single-cell biophysical phenotyping and classification of breast cancer cell types

We next sought to test if the single-cell biophysical phenotypic profiles generated by FACED-QPI could achieve the power required for cell-type classification. Based on visual assessment of the randomly selected single-cell DPC and quantitative phase images [Fig. 4(a)], each cell type exhibited some degree of heterogeneity in cell size, shape, and phase distribution. However, no trivial difference in cell morphologies between the two types was visually discerned. Nevertheless, the high-dimensional hierarchical biophysical profiles (normalized based on the z-score) extracted from

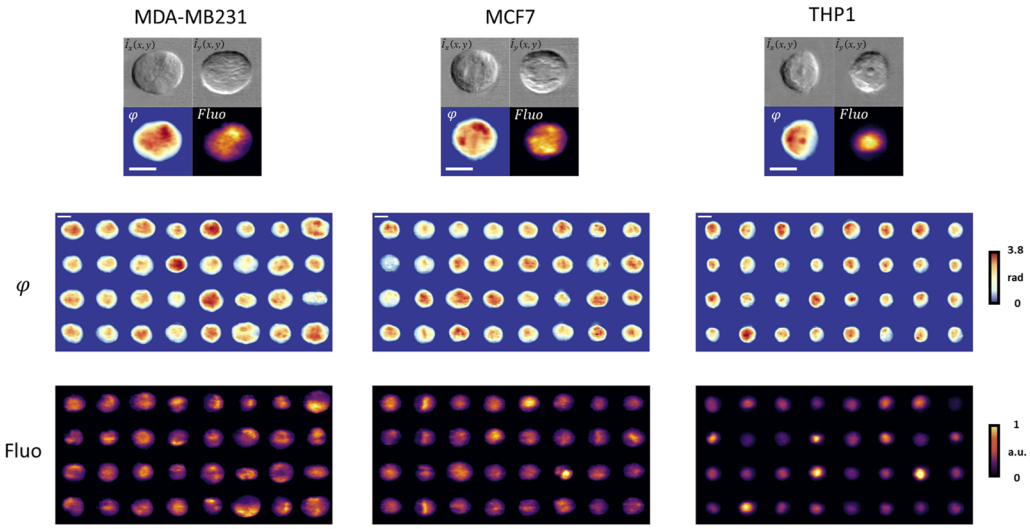

FIG. 3. Examples of different imaging contrasts captured by the multimodal FACED IFC platform: quantitative phase (φ) and fluorescence (Fluo) images. Three different cell types were used in this demonstration: human leukemic monocyte (THP-1) and two different breast cancer cells (MDA-MB231 and MCF7). The scale bars represent 10 μm.

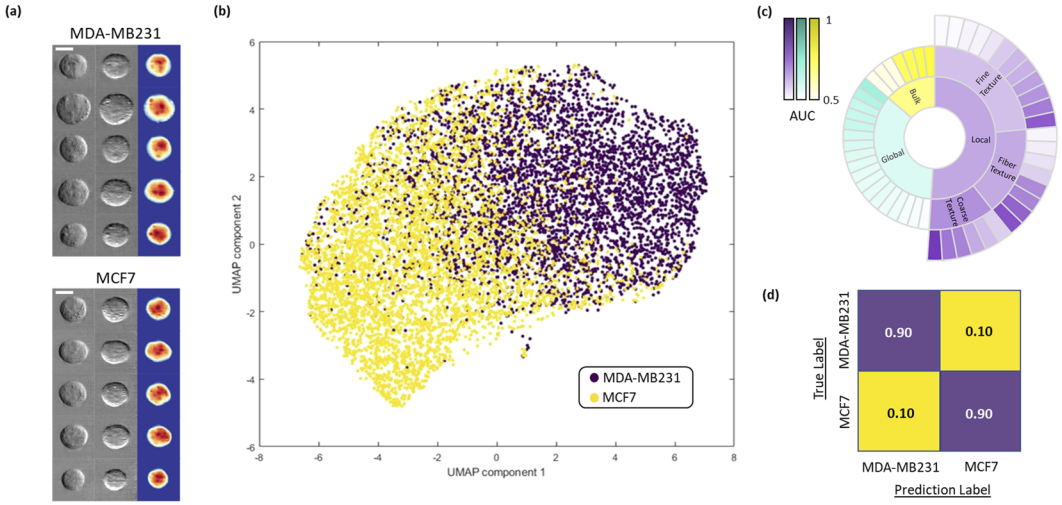

FIG. 4. Label-free classification of breast cancer cell sub-types based on FACED-QPI. (a) Representative single-cell FACED images [left: $\hat{I}_x(x,y)$, middle: and $\hat{I}_y(x,y)$ and right: QPI] of MDA-MB231 and MCF7 captured by using the multimodal FACED IFC platform. The scale bars represent 10 μm. (b) A UMAP plot (n = 4391 for MDA-MB231 and n = 4314 for MCF7) was constructed based on the high-dimensional biophysical phenotypes (see the supplementary material, Note 1), and the two clusters, which represent the two breast cancer cell sub-types, are distinguishable. (c) A sunburst chart showing the significance of the hierarchical biophysical phenotypic profile in classification between MDA-MB231 and MCF7. (d) A confusion matrix of the neural-network-based classification model trained with the full set of biophysical features extracted from the quantitative phase images of MDA-MB231 and MCF7.

the FACED-QPI allowed us to clearly distinguish the two populations, which are separable in the 2D cluster plot generated by a dimensionality-reduction algorithm, called UMAP[21] [Fig. 4(b)]. Based on the receiver operating characteristic analysis, we further identified that features of phase (or dry mass density) texture are among the top 10 features most responsible for distinguishing the two cell types (e.g., phase entropy mean referred to as coarse texture, whereas phase fiber variance is the fiber texture) [Fig. 4(c); see the fully annotated biophysical profile in the supplementary material, Fig. S7]. In order to quantify the classification performance, we used a full set of high-resolution single-cell biophysical profiles to train a deep neural network model for classifying the two breast cancer cell types. The overall classification accuracy is as high as 90% [Fig. 4(d)].

C. Label-free cell-cycle progression tracking

The gold standard for identifying cell-cycle phases (G1, S, and G2/M) is based on quantifying the fluorescence intensity given by the DNA dye.[22] Recent advancements in IFC have shown the feasibility of using label-free single-cell bright-field and dark-field images to predict DNA content and thus the cell cycle phases of live cells.[3] The underlying rationale is to maximize the information content of cytometric analysis with a minimum number of fluorescence labels bypassing the limitations due to multi-color fluorescence measurements, e.g., costly and laborious labeling protocols and fluorescence spectral overlap (crosstalk). Going beyond, here, we investigated if the large-scale single-cell quantitative phase information extracted by FACED-QPI could provide sufficient statistical power to track the cell cycle progression, discern the key cell-cycle phases, and analyze subcellular cell mass texture changes if any.

Based on the co-registered quantitative phase and fluorescence images of the same cells [Figs. 5(a) and 5(f)], we performed a linear regression analysis and showed a high correlation between all the biophysical phenotypes and the integrated fluorescence intensity given by the DNA label (Spearman's correlation r = 0.824 for MDA-MB231 and r = 0.772 for MCF7) [Figs. 5(b) and 5(g)]. Using a CNN-based regression model, we were also able to predict the DNA content based on the FACED-QPI along with a high correlation (Pearson's correlation > 0.7 for both MDA-MB231 and MCF7) with the true DNA content given by the fluorescence images (see the supplementary material, Figs. S8a and S8b). To further analyze the biophysical profiles, we identified that the bulk features (cell area, volume, and dry mass) and the subcellular phase textures (reflected by phase entropy radial distribution, phase fiber radial distribution, and fit texture mean) consistently rank among the top in the correlation with the integrated fluorescence intensity [Figs. 5(c) and 5(h)]. It is consistent with the fact that cell scales its size to cope with the gain in dry mass during cell growth.[23] In addition, re-organization of subcellular components also occurs during cell cycle (e.g., actin and microtubule depolymerization and chromatin condensation) that leads to a change in subcellular dry mass density distribution.

Applying the Watson pragmatic fitting method,[20] we also showed that our FACED-QPI data could estimate the population size in each cell cycle phase (i.e., G1, S, and G2/M) with good agreements with the ground truth defined by the fluorescence DNA label [Figs. 5(d) and 5(i)]. We note that multi-color fluorescence labeling could further provide an improved "ground truth", which better distinguishes different cell-cycle phases, especially the S-phase (for example, three-color FUCCI labeling[24]). Plotting the high-dimensional biophysical phenotypic data in a lower-dimensional (i.e., 3D) space based on a method called PHATE,[25] we also observed a clear continuous trajectory progressing from G1 to S to G2/M

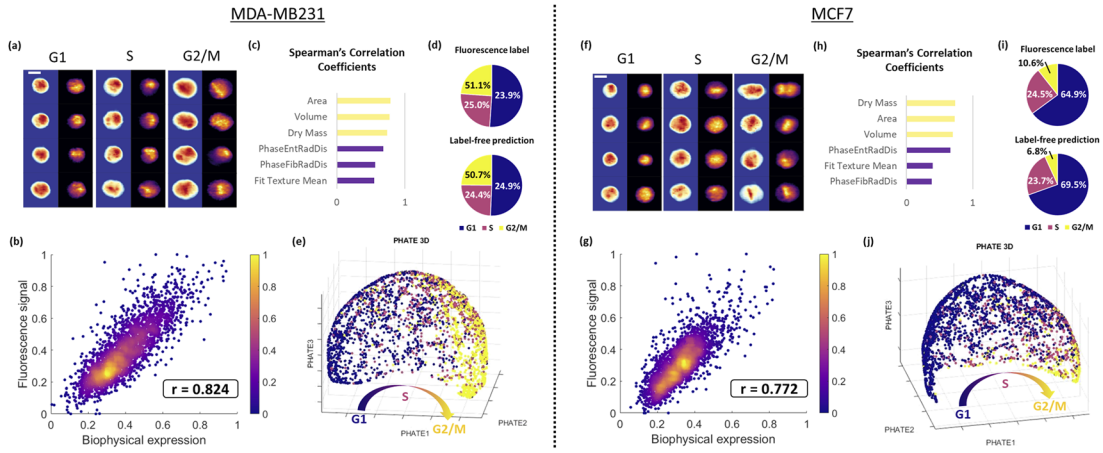

FIG. 5. Label-free cell-cycle progression tracking using the multimodal FACED IFC platform. The analysis was performed on two different breast cancer types: (a)–(e) MDA-MB231 and (f)–(j) MCF7. [(a) and (f)] Representative single-cell images (left: QPI; right: fluorescence) captured by using the multimodal FACED IFC platform. The scale bars represent 10 μm. [(b) and (g)] Correlation between the biophysical phenotypes extracted from the FACED-QPI and integrated fluorescence intensity computed from the FACED fluorescence images. A linear regression model was used to fit all the 51 biophysical phenotypes to the integrated fluorescence intensity, and thus, the plots display the integral correlative relationship between the biophysical phenotypes and the fluorescence intensity. r represents the Spearman's correlation coefficient. [(c) and (h)] Ranking of correlation (based on Spearman's correlation coefficient) between individual biophysical phenotype (top 6) and the integrated fluorescence intensity. The bar colors, which denote the types of phenotypes, can be referred to the color scheme of Fig. 4(c). [(d) and (i)] Comparison between the predicted proportions of G1, S, and G2/M phases with the ground truth defined by the fluorescence DNA label. [(e) and (j)] The PHATE 3D plots (n = 2724 for MDA-MB231 and n = 2763 for MCF7) are constructed based on the high-dimensional biophysical phenotypes, and cell-cycle progression can be clearly visualized (the colors denote the three cell cycle phases). For MDA-MB231 and MCF7, n = 1392, 681, 651 and n = 1793, 677, 293 for G1, S, and G2/M phases, respectively.

phase [Figs. 5(e) and 5(j)]. While the previous QPI work has primarily focused on analyzing the variation of a handful of bulk biophysical features (e.g., cell mass[23]) during cell growth, quantitative analysis of predicting cell cycle stages and visualizing the progression [Figs. 5(e) and 5(j)] involving high-dimensional biophysical profiles have remained challenging. It is arguably because of the lack of the required combination of the QPI throughput and content. These results suggest that FACED-QPI data could offer the statistical power needed for gaining the mechanistic understanding of cell behaviors.

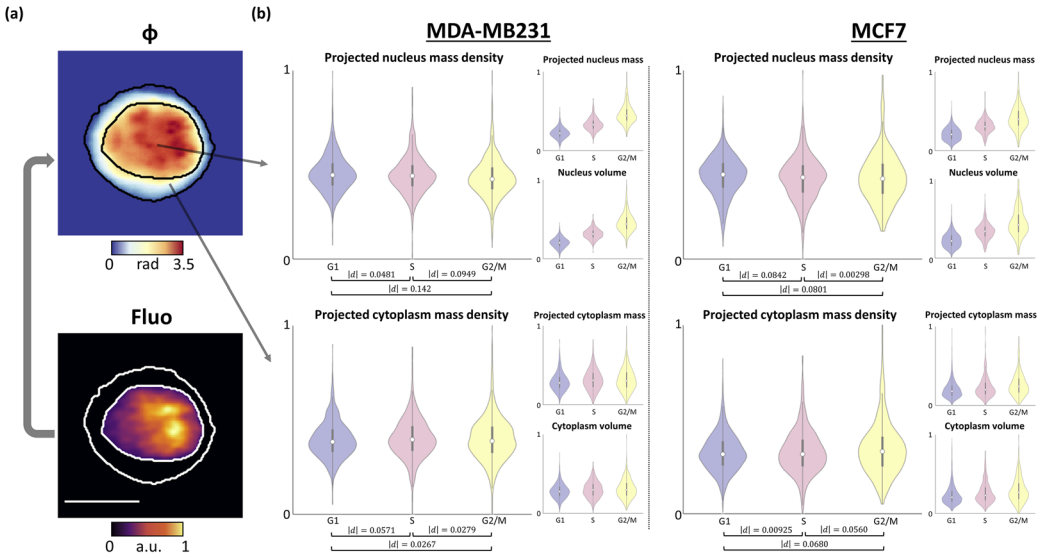

FIG. 6. Compartment-specific cell-cycle analysis. (a) An example of paired single-cell image (quantitative phase and fluorescence) showing the masked regions of nucleus and cytoplasm. The scale bar represents 10 μm. (b) The distribution of normalized single-cell volume, projected mass, and projected mass density of both nucleus and cytoplasm in MDA-MB231 and MCF7, respectively, across the three cell cycle phases, i.e., G1, S, and G2/M phase. $|d|$ represents the Cliff's delta value.

D. Compartment-specific cell-cycle analysis

To further leverage the multimodal imaging capability, we correlated the QPI of cells with fluorescence images for analyzing the biophysical characteristics of the two key sub-cellular compartments separately during cell cycle. Specifically, we used the QPI and DNA-labeled fluorescence image to determine the cell body and nucleus region of each cell. Thus, we could define the binary masks enclosing the nucleus and the cytoplasmic compartments in each single-cell QPI [Fig. 6(a)]. Assuming these compartments in an ellipsoidal shape as cells flowed in suspension,[10] we could estimate the dry mass (DM) of the compartments by integrating the dry mass density (DMD) within the corresponding ellipsoidal volumes (see the supplementary material, Note 1). In this study, we focused on the relative changes in volume, DM, and DMD, rather than their absolute values during the cell cycle.

We observed that both the nucleus and cytoplasm grow in dry mass (from G1, S to G2/M phase) and the increasing trends tightly follow the increase in the nucleus/cytoplasm volume. This is consistent with the cell growth in G1 and G2 phases and replication of genetic material in the S phase. More interestingly, we found that the DMD of both nucleus and cytoplasm is highly conserved across the three cell cycle phases, i.e., G1, S, and G2/M [Fig. 6(b)]. Our effect size analysis showed that there is no statistically significant difference (i.e., Cliff's delta value $|d| < 0.147$) among the mass density of cells in different cell cycle phases. The same observation applied to two different types of breast cancer cells, MDA-MB231, and MCF-7 [Fig. 6(b)]. This coincides with the recent study[23] that suggests an underlying mechanism tightly controlling the change in both cell size and cellular contents such that homeostasis of mass density is achieved in both the nucleus and cytoplasm of cells.

IV. CONCLUDING REMARK

By leveraging an all-optical passive laser scanner based on FACED, we have demonstrated a high-throughput QPI modality that achieves an ultrafast imaging line-scan rate beyond MHz and preserves the subcellular resolution. Supported by our theoretical framework and experimental validation, we showed that this FACED-QPI method retrieves the quantitative phase through high-speed multiplexed DPC captures. This multiplexing scheme is based on precisely time-interleaving two line-scan replicas, which contain two sets of orthogonal spatial phase gradient information. This method enables ultrafast QPI at least 100 times faster than the available QPI methods that rely on camera technology for image capture. We note that although the state-of-the-art high-speed camera can, in principle, achieve an imaging speed at >100 000 fps, strong illumination is generally required to combat the loss of sensitivity at high speed. Thus, it may not be favorable for live-cell imaging. We also note that a similar DPC-based QPI has recently been adopted in time-stretch microscopy[14] in our previous work and has successfully been employed as a high-throughput imaging flow cytometer for cell-type classification[2] and drug–response assay.[19] Nevertheless, wide adoption of time-stretch-based QPI in cellular imaging assay still remains limited. This is due to the fact that time-stretch-based QPI has primarily been relying on fiber technology that does not offer a sufficiently high dispersion-to-loss ratio, and thus high image fidelity, for high-speed, high-resolution fluorescence imaging in the visible spectrum. In contrast, by bypassing the use of fiber and its limitation, here, we have demonstrated synchronized and co-registered FACED-QPI and fluorescence imaging and applied this multimodal system in IFC at an imaging throughput of 77 000 cells/s.

Specifically, we established the high-dimensional biophysical profiles for individual cells extracted from FACED-QPI and analyzed them with the deep-learning pipelines. We have shown that this deep-learning-assisted biophysical profiling not only shows sufficient label-free statistical power to classify two cancer cell subtypes but also predicts cell-cycle phases with high accuracy comparable to the gold-standard fluorescence method. Furthermore, the co-registered subcellular information obtained from FACED-QPI and fluorescence images allowed us to perform correlative, compartment-specific (nucleus and cytoplasm in this study) analysis of the spatially resolved biophysical profiles during cell cycle progression.

We note that the current platform can readily be extended to multi-color fluorescence imaging combined with FACED-QPI (with multiple and/or wavelength-tunable laser sources, as well as careful design of fluorescence labeling panels). The single-cell biophysical profiling strategy presented in this work can also be applicable and extended to many existing deep learning pipelines,[26,27] involving supervised feature selection (e.g., Cell Profilers[28]) or unsupervized latent feature generation (e.g., auto-encoders[29]).

The capability of simultaneously capturing QPI and fluorescence images of single cells at high throughput could open a new paradigm to comprehensive image-based profiling of cellular phenotypes. It could result in a new repertoire of the single-cell library for systematic understanding of the correlations between biophysical and biochemical information of cells in response to different stimulations or perturbation,[30] e.g., screening of genetically altered cells.[31]

SUPPLEMENTARY MATERIAL

See the supplementary material for the table of all extracted biophysical phenotypes (including the corresponding equations), detailed derivation of phase retrieval in FACED-QPI, full schematic of the optical setup, results of phase calibration, measurement of phase noise, architecture of the neural networks, significance of every biophysical phenotype (fully annotated) in cell-type classification, and correlation between the predicated and actual DNA content.

ACKNOWLEDGMENTS

This work was supported by the Research Grants Council of the Hong Kong Special Administrative Region of China (Grant Nos. 17208918, 17209017, 17259316, RFS2021-7S06, and C7047-16G).

DATA AVAILABILITY

The data that support the findings of this study are available from the corresponding author upon reasonable request.

REFERENCES

[1] L. F. Ogle, J. G. Orr, C. E. Willoughby, C. Hutton, S. McPherson, R. Plummer, A. V. Boddy, N. J. Curtin, D. Jamieson, and H. L. Reeves, J. Hepatol. **65**, 305 (2016).

[2]K. C. M. Lee, M. Wang, K. S. E. Cheah, G. C. F. Chan, H. K. H. So, K. K. Y. Wong, and K. K. Tsia, Cytometry, Part A **95**, 510 (2019).
[3]T. Blasi, H. Hennig, H. D. Summers, F. J. Theis, J. Cerveira, J. O. Patterson, D. Davies, A. Filby, A. E. Carpenter, and P. Rees, Nat. Commun. **7**, 10256 (2016).
[4]U. Kubitscheck, *Fluorescence Microscopy: From Principles to Biological Applications*, 2nd ed. (John Wiley & Sons, 2017).
[5]H. Subramanian, P. Pradhan, Y. Liu, I. R. Capoglu, X. Li, J. D. Rogers, A. Heifetz, D. Kunte, H. K. Roy, A. Taflove, and V. Backman, Proc. Natl. Acad. Sci. U. S. A. **105**, 20118 (2008).
[6]J. M. Phillip, P.-H. Wu, D. M. Gilkes, W. Williams, S. McGovern, J. Daya, J. Chen, I. Aifuwa, J. S. H. Lee, and R. Fan, Nat. Biomed. Eng. **1**, 0093 (2017).
[7]M. M. Stevens, C. L. Maire, N. Chou, M. A. Murakami, D. S. Knoff, Y. Kikuchi, R. J. Kimmerling, H. Liu, S. Haidar, N. L. Calistri, N. Cermak, S. Olcum, N. A. Cordero, A. Idbaih, P. Y. Wen, D. M. Weinstock, K. L. Ligon, and S. R. Manalis, Nat. Biotechnol. **34**, 1161 (2016).
[8]S. Cohen-Maslaton, I. Barnea, A. Taieb, and N. T. Shaked, J. Biophotonics **13**, e202000117 (2020).
[9]K. Kim, W. S. Park, S. Na, S. Kim, T. Kim, W. Do Heo, and Y. Park, Biomed. Opt. Express **8**, 5688 (2017).
[10]G. Dardikman, Y. N. Nygate, I. Barnea, N. A. Turko, G. Singh, B. Javidi, and N. T. Shaked, Biomed. Opt. Express **9**, 1177 (2018).
[11]C. Liu, M. Malek, I. Poon, L. Jiang, A. M. Siddiquee, C. J. R. Sheppard, A. Roberts, H. Quiney, D. Zhang, X. Yuan, J. Lin, C. Depeursinge, P. Marquet, and S. S. Kou, Photonics Res. **7**, 1042 (2019).
[12]M. Schürmann, G. Cojoc, S. Girardo, E. Ulbricht, J. Guck, and P. Müller, J. Biophotonics **11**, e201700145 (2018).
[13]J. Wu, Y. Xu, J. Xu, X. Wei, A. C. S. Chan, A. H. L. Tang, A. K. S. Lau, B. M. F. Chung, H. C. Shum, E. Y. Lam, K. K. Y. Wong, and K. K. Tsia, Light Sci. Appl. **6**, e16196 (2017).
[14]K. C. M. Lee, A. K. S. Lau, A. H. L. Tang, M. Wang, A. T. Y. Mok, B. M. F. Chung, W. Yan, H. C. Shum, K. S. E. Cheah, and G. C. F. Chan, J. Biophotonics **12**, e201800479 (2019).
[15]B. Guo, C. Lei, Y. Wu, H. Kobayashi, T. Ito, Y. Yalikun, S. Lee, A. Isozaki, M. Li, Y. Jiang, A. Yasumoto, D. Di Carlo, Y. Tanaka, Y. Yatomi, Y. Ozeki, and K. Goda, Methods **136**, 116 (2018).
[16]A. B. Parthasarathy, K. K. Chu, T. N. Ford, and J. Mertz, Opt. Lett. **37**, 4062 (2012).
[17]Q. T. K. Lai, G. G. K. Yip, J. Wu, J. S. J. Wong, M. C. K. Lo, K. C. M. Lee, T. T. H. D. Le, H. K. H. So, N. Ji, and K. K. Tsia, Nat. Protoc. (in press) (2021).
[18]M. Wang, K. C. M. Lee, B. M. F. Chung, S. V. Bogaraju, H.-C. Ng, J. S. J. Wong, H. C. Shum, K. K. Tsia, and H. K.-H. So, "High-speed laser-scanning biological microscopy using FACED," IEEE Trans. Neural Networks Learn. Syst. (published online) (2021).
[19]D. M. D. Siu, K. C. M. Lee, M. C. K. Lo, S. V. Stassen, M. Wang, I. Z. Q. Zhang, H. K. H. So, G. C. F. Chan, K. S. E. Cheah, and K. K. Y. Wong, Lab Chip **20**, 3696 (2020).
[20]J. V. Watson, S. H. Chambers, and P. J. Smith, Cytomery J. Int. Soc. Anal. Cytol. **8**, 1 (1987).
[21]L. McInnes, J. Healy, N. Saul, and L. Großberger, J. Open Source Software **3**, 861 (2018).
[22]Z. Darzynkiewicz, X. Huang, and H. Zhao, Curr. Protoc. Immunol. **119**, 5 (2017).
[23]K. Kim and J. Guck, Biophys. J. **119**, 1946 (2020).
[24]A. Sakaue-Sawano, H. Kurokawa, T. Morimura, A. Hanyu, H. Hama, H. Osawa, S. Kashiwagi, K. Fukami, T. Miyata, H. Miyoshi, T. Imamura, M. Ogawa, H. Masai, and A. Miyawaki, Cell **132**, 487 (2008).
[25]K. R. Moon, D. van Dijk, Z. Wang, S. Gigante, D. B. Burkhardt, W. S. Chen, K. Yim, A. van den Elzen, M. J. Hirn, R. R. Coifman, N. B. Ivanova, G. Wolf, and S. Krishnaswamy, Nat. Biotechnol. **37**, 1482 (2019).
[26]M. Kräter, S. Abuhattum, D. Soteriou, A. Jacobi, T. Krüger, J. Guck, and M. Herbig, Adv. Sci. **8**, 2003743 (2021).
[27]M. Doan, J. A. Sebastian, J. C. Caicedo, S. Siegert, A. Roch, T. R. Turner, O. Mykhailova, R. N. Pinto, C. McQuin, A. Goodman, M. J. Parsons, O. Wolkenhauer, H. Hennig, S. Singh, A. Wilson, J. P. Acker, P. Rees, M. C. Kolios, and A. E. Carpenter, Proc. Natl. Acad. Sci. U. S. A. **117**, 21381 (2020).
[28]C. McQuin, A. Goodman, V. Chernyshev, L. Kamentsky, B. A. Cimini, K. W. Karhohs, M. Doan, L. Ding, S. M. Rafelski, D. Thirstrup, W. Wiegraebe, S. Singh, T. Becker, J. C. Caicedo, and A. E. Carpenter, PLoS Biol. **16**, e2005970 (2018).
[29]Y. Zhou, A. Yasumoto, C. Lei, C.-J. Huang, H. Kobayashi, Y. Wu, S. Yan, C.-W. Sun, Y. Yatomi, and K. Goda, eLife **9**, e52938 (2020).
[30]K. C. M. Lee, J. Guck, K. Goda, and K. K. Tsia, "Toward deep biophysical cytometry: Prospects and challenges," Trends Biotechnol. (published online) (2021).
[31]M. Lawson and J. Elf, Nat. Methods **18**, 358 (2021).